A methodical quantification of needle visibility and echogenicity in ultrasound images

van de Berg, Nick J.; Sánchez-Margallo, Juan A.; van Dijke, Arjan P.; Langø, Thomas; van den Dobbelsteen, John J.

DOI
10.1016/j.ultrasmedbio.2018.10.004

Publication date
2019

Document Version
Final published version

Published in
Ultrasound in Medicine and Biology

Citation (APA)
van de Berg, N. J., Sánchez-Margallo, J. A., van Dijke, A. P., Langø, T., & van den Dobbelsteen, J. J. (2019). A methodical quantification of needle visibility and echogenicity in ultrasound images. *Ultrasound in Medicine and Biology*, *45*(4), 998-1009. https://doi.org/10.1016/j.ultrasmedbio.2018.10.004

Important note
To cite this publication, please use the final published version (if applicable).
Please check the document version above.

Ultrasound in Med. & Biol., Vol. 45, No. 4, pp. 998–1009, 2019

0301-5629/$ - see front matter

https://doi.org/10.1016/j.ultrasmedbio.2018.10.004

● *Original Contribution*

A METHODICAL QUANTIFICATION OF NEEDLE VISIBILITY AND ECHOGENICITY IN ULTRASOUND IMAGES

Nick J. van de Berg,* Juan A. Sánchez-Margallo,†,‡ Arjan P. van Dijke,* Thomas Langø,† and John J. van den Dobbelsteen*

* Department of BioMechanical Engineering Delft University of Technology, Delft, The Netherlands; † Medical Technology, SINTEF, Norway; and ‡ Computer Systems and Telematics, University of Extremadura, Extremadura, Spain

(*Received* 6 *April* 2018; *revised* 31 *August* 2018; *in final from* 4 *October* 2018)

Abstract—During ultrasound-guided percutaneous interventions, needle localization can be a challenge. To increase needle visibility, enhancements of both the imaging methods and the needle surface properties have been investigated. However, a methodical approach to compare potential solutions is currently unavailable. The work described here involves automated image acquisition, analysis and reporting techniques to collect large amounts of data efficiently, delineate relevant factors and communicate effects. Data processing included filtering, line fitting and image intensity analysis steps. Foreground and background image samples were used to compute a contrast-to-noise ratio or a signal ratio. The approach was evaluated in a comparative study of commercially available and custom-made needles. Varied parameters included needle material, diameter and surface roughness. The shafts with kerfed patterns and the trocar and chiba tips performed best. The approach enabled an intuitive polar depiction of needle visibility in ultrasound images for a large range of insertion angles. (E-mail: n.j.p.vandeberg@tudelft.nl) © **2018 The Author(s). Published by Elsevier Inc. on behalf of World Federation for Ultrasound in Medicine & Biology. This is an open access article under the CC BY-NC-ND license. (http://creativecommons.org/licenses/by-nc-nd/4.0/).**

Key Words: **Ultrasound, Echogenicity, Visibility, Needle interventions, Experimental methods, Contrast-to-noise ratio, Signal ratio, High-echoic range, Polyvinyl alcohol.**

INTRODUCTION

Clinical background

Percutaneous needle interventions are commonly used for the local diagnosis and treatment of deep-seated tissue structures, such as lesions suspected of being cancerous. Exemplar interventions include taking a biopsy and treating tissue by radiofrequency ablation, during which accurate needle placement is crucial. Imaging techniques, such as ultrasound (US), computed tomography and magnetic resonance imaging, provide guidance and enable the inspection of lesion geometry and position (Kunzli et al. 2011).

Needle localization in US images

About 70% of (interventional) radiologists have reported that targeting in percutaneous interventions can be complicated by poor needle visibility (de Jong et al. 2018). Both the shaft and tip localization in the US frame can be a challenge. Complicating factors can be suboptimal needle echogenicity, image plane alignment difficulties and imaging artifacts, such as reverberations, comet tails and shadowing effects (Chapman et al. 2006). Pragmatic strategies to assess tip location include rocking the transducer, advancing the instrument and injecting fluids (Chapman et al. 2006). Although these dynamics-based strategies are effective, it would be better to improve needle visibility without movement.

To enhance needle visibility, both the imaging techniques and the needles themselves can be improved. Beam steering can be used to increase the return rate of reflections from the needle surface back to the US transducer (Baker et al. 1999). Spatial compound imaging has a similar effect (Cohnen et al. 2003; Wiesmann et al. 2013). No apparent beneficial results were, however, obtained with the use of frequency compound imaging or harmonic imaging techniques (Mesurolle et al. 2006). In all, the most dramatic improvements came from

Address correspondence to: Nick J. van de Berg, Department of BioMechanical Engineering Delft University of Technology, Mekelweg 2, Delft 2628CD, The Netherlands. E-mail: n.j.p.vandeberg@tudelft.nl

adaptations of the needle surface (Nichols et al. 2003), by means of coating (de Korte et al. 2012; Gottlieb et al. 1998), material scoring (Charboneau et al. 1990), denting (Miura et al. 2014) or introducing screw or sawtooth patterns (Bigeleisen et al. 2016; Reading et al. 1987). Finally, tip localization in color Doppler mode can be improved by actively vibrating the needle during use (Adebar et al. 2014; Cabreros et al. 2015; Harmat et al. 2006; Klein et al. 2007).

Related work

An overview of previously adopted experimental methods used to quantify and compare proposed needle visibility enhancing techniques is provided in Table 1. These methods assess regions of interest on the needle surface—the image foreground (FG). Shown are the measurement techniques, the metrics used and the establishment of a reference area in the image with which the needle is compared—the image background (BG). Examples of well-defined BG areas include the full US image masked by the FG (Bigeleisen et al. 2016), an image sample of homogeneous tissue structures collected adjacent to the needle (Culp et al. 2000) and a fixed-size image sample collected directly above the needle (Nakagawa et al. 2015).

Table 1 further outlines the use of the words *visibility* and *echogenicity* as metrics in these studies. Different measurement techniques have been associated with either one of these metrics, suggesting that visibility and echogenicity have not been clearly delineated in the literature. In this article, the terms *visibility* and *echogenicity* are distinct factors in the quantitative assessment of imaged needles. The following etymology-based definitions are employed: *visibility* is the ability to be seen, and *echogenicity* is the ability to generate (sound) reflections.

Because sound reflections are visualized in an US image, it is clear that these terms are related. Nevertheless, a surface that reflects strong signals may still not be clearly visible in the image. A visible surface must produce echoes *differently* from its surroundings; that is, the FG and BG areas must be segregable. The contrast-to-noise ratio (CNR) (Arif et al. 2018) aptly quantifies surface visibility as it evaluates the difference in signal strengths. In turn, echogenicity resembles a surface property, independent of BG conditions. A signal ratio (SR) can be used to relate the FG signal strength to that of a reflection standard.

Aim and approach

Many solutions have been proposed to improve needle visibility in US images. However, an objective and efficient approach for the evaluation of their efficacy is currently lacking. Functional assessments will enable comparative studies and guide advancements in this field. This article describes a novel approach to comparing needle visibility and echogenicity in US images. The data acquisition and analysis methods were largely automated. Instead of reintroducing the needle in numerous relevant orientations, a rotational platform was used to study a full range of insertion angles. Needle visibility was analyzed in polyvinyl alcohol (PVA), which has good tissue resemblance in US images (Arif et al. 2018; Surry et al. 2004). Needle echogenicity was analyzed in water to reduce attenuations and distortions. Per video, a selection of frames were subjected to tip search algorithms, yielding image FG and BG samples and CNR/SR values. The approach was assessed in a comparative study of various needle surface treatments.

Table 1. Studies on needle visibility or echogenicity in ultrasound images. The columns describe the measurement techniques, the used metrics and the backgrounds (BG). The strictness in defining BG areas is divided in three categories: I denotes an undefined area, which typically includes image ratings by experts, II denotes an area with a defined size, and III denotes an area with a defined size and location.

	Metric		
Technique	Visibility	Echogenicity	Background
Image rating	Mesurolle et al. 2006 Gofeld et al. 2013 Uppal et al. 2014	Sviggum et al. 2013 Mariano et al. 2014	I
Video rating	Maecken et al. 2007 Guo et al. 2012 Munirama et al. 2015	Fuzier et al. 2015	I
Inter-procedural rating	Gottlieb et al. 1998 Bergin et al. 2002		I
Spatial detectability	Edgcombe and Hocking 2010 Hebard et al. 2011		I
Temporal detectability	Kilicaslan et al. 2014 Abbal et al. 2015		I
Image intensity analysis	Schafhalter-Zoppoth et al. 2004 Arif et al. 2018		II
	Nakagawa et al. 2015 Bigeleisen et al. 2016	Culp et al. 2000 Nichols et al. 2003	III

To allow evaluation, reproduction and extension of the proposed methods and results, all of the associative files, the data, the MATLAB and C (Arduino) codes and the CAD models for 3-D printed and laser cut parts will be made open source (available at: github.com/misitlab/needles-in-ultrasound).

METHODS

To study the visibility and echogenicity of needles, two measurement platforms were constructed (Fig. 1), both containing a curved array transducer (C5-2, Philips, Amsterdam, Netherlands) connected to the US system (HD7 XE, Philips, Amsterdam, Netherlands) and a video (MPEG-4) capturing device (USB3HDCAP, StarTech, Lockbourne, OH, USA). This transducer type is commonly used in abdominal interventions. The US system was set to a frequency of 5 MHz, an imaging depth of 15 cm and a focus depth of 9 cm. The gain setting was varied per setup (PVA: gain = 25, water: gain = 0) to visually match the image intensity at the depth of focus.

Both platforms included a stepper motor (42BYGHM809, Wantai Motor, Jiangsu, China) that was coupled to the needle via a fixture or needle template. The motor enabled needle rotations in the longitudinal imaging plane, simulating the variation of insertion angles. The motor was connected to a microstepping driver (Big Easy Driver, Sparkfun, Boulder, CO, USA) and operated at a constant angular speed of 0.1 rad/s (100 steps/s with 6400 steps in 2π rad), using a microcontroller board (Arduino Uno R3, Arduino, Ivrea, Italy). The insertion angle range was limited to 25°, ..., 180° by the needle–transducer contact.

Two cylindrical PVA specimens with a radius and height of 100 mm were prepared for the visibility study. One is illustrated in Figure 1 (left). Needles were inserted to a depth of 100 mm, so that their tips coincided approximately with the cylinder axis. A needle template had holes at every 10 mm along the specimen height and ensured an even distribution of insertion paths. The transducer height was adjustable by means of an all-thread rod, which enabled the alignment with the needle. The transducer was fixed to a linear micro-stage (PT1/M, Thorlabs, Newton, NJ, USA) to ensure contact between the transducer and the specimen.

During the echogenicity study, the measurement platform in Figure 1 (right) was below the water. Motor shaft rotations were transmitted with a timing belt and two equal-sized pulleys. The pulley that was below water level had its rotational axis aligned with the focus depth of the US transducer and with the FG on the needle shaft.

Specimens

A 4 m% (percentage by mass) super-hydrolyzed PVA (Selvol PVOH 165, Sekisui Chemical Group, Secaucus, NJ, USA), 1 m% scattering agent (Silica gel 60, Merck Sharp & Dohme [MSD], Haar, Germany) solution in water was used for the visibility study. Specimens were subjected to two freeze–thaw cycles, according to the protocol in (de Jong et al. 2017), aimed to mimic human liver tissue.

The water container floor and walls were outside the US field of view. A polished stainless-steel plate

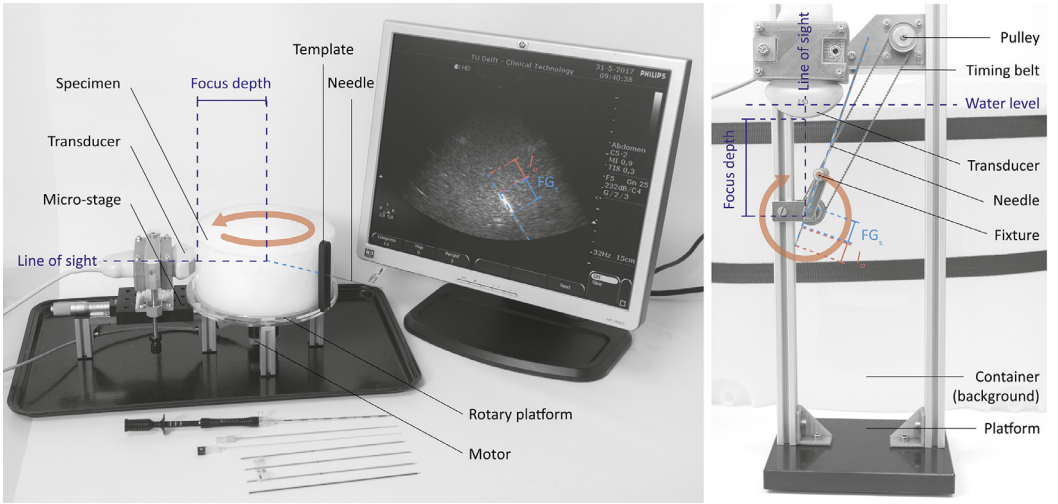

Fig. 1. Left: Needle visibility was analyzed in a polyvinyl alcohol specimen placed on top of a rotary platform. Needles were inserted through a template to a depth where the tip coincided with the rotational axis of the platform and with the depth of focus of the ultrasound transducer. The needle shaft FG_s was analyzed at a variable offset (l_0) from the tip. Right: Needle echogenicity was analyzed in a water-filled container. A stepper motor (hidden behind the top pulley) actuated a timing belt. A second pulley, providing the axis of rotation of the needle, was submerged and located at the depth of focus of the transducer. An off-axis fixture enabled a clear view of the needle from all angles.

(10 × 10 × 2 mm) was used as a reference specimen to approximate a reflection optimum. This specimen was positioned at the focus depth, facing the transducer, resulting in high specular reflections and a bright white area in the image.

Needles and surface treatments

Six of the included needles, illustrated in Figure 2, were custom-made, whereas two were commercially available: an 18G needle (Trocar, Cook Medical, Bloomington, IN, USA) and a 22G needle (Chiba, Angiomed, Karlsruhe, Germany). The material surface was treated by means of polishing (Nos. 1 and 2), sand blasting (No. 4) or electric discharge machining (EDM, Nos. 5and 6). The patterns kerfed in the EDM-treated needles were selected for their resemblance to compliant joints in steerable needle designs (Henken et al. 2017; van de Berg et al. 2017). Both kerf types were of equal size (width = 0.1 mm, depth = 0.5 mm), but the second had additional beveled edges (45° × 0.2 mm), which may increase the specular reflections for a specific insertion angle range. Other relevant production details are listed in Figure 2 and Table 2, where the arithmetic average roughness values, R_a, were obtained over a length of 10 mm, using a surface roughness tester (Surftest SJ-301, Mitutoyo, Kawasaki, Kanagawa, Japan).

Image acquisition

The experiments in water and PVA were conducted in sequence. Per experiment and needle type, 10 videos of needle rotations in the longitudinal imaging plane were acquired. The experimental design incorporated a randomization of needle types.

Videos were processed in MATLAB (R2017b, The MathWorks, Natick, MA, USA). The constants used are listed in Table 3. A manual segmentation step was performed for two image frames that were collected at one-fifth and four-fifths of the video duration (Fig. 3). The segmented needle orientations were used to synchronize the video duration with the angular needle motion. A linear inter- and extrapolation yielded the frames for the "insertion angle" range $\Delta\theta = 25^\circ, 30^\circ, \ldots, 180^\circ$. At 180°, the needle tip pointed toward the transducer. For larger angles, an imaging symmetry was assumed. Next, the average of the manually segmented tip positions was used to estimate the center of rotation (CoR) of the

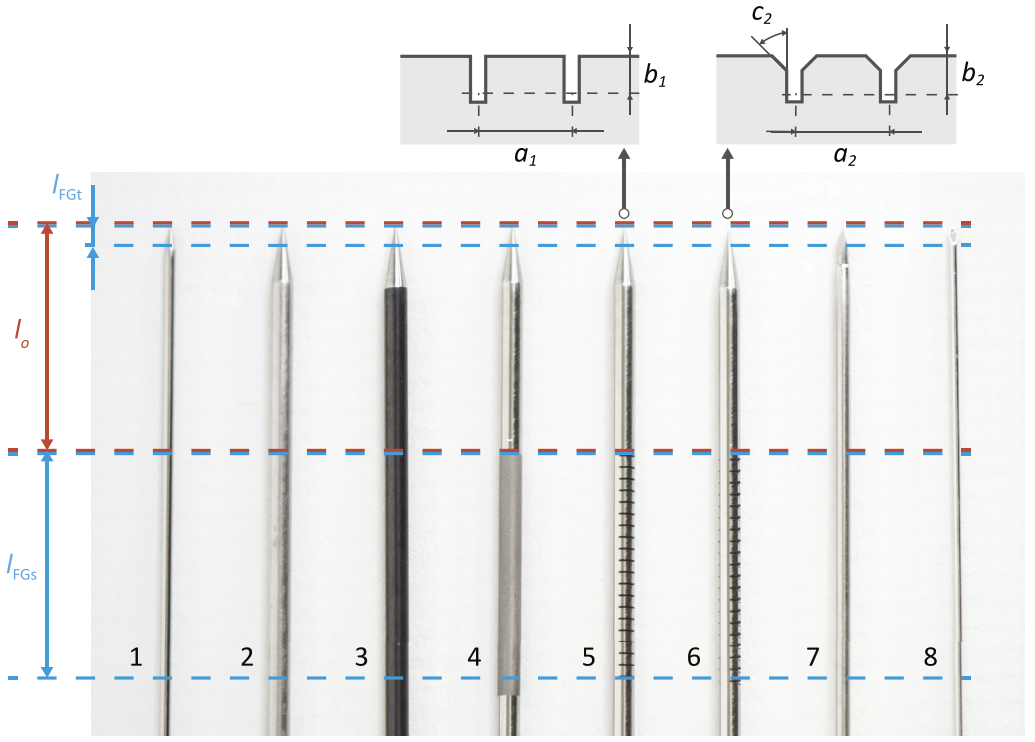

Fig. 2. Six manufactured (1–6) and two commercially available (7, 8) needles were used. Needles 4–6 were treated at a distance $l_0 = 20$ mm from the tip. All needles were analyzed over the lengths $l_{FGt} = 2$ mm and $l_{FGs} = 20$ mm. The kerfs (5, 6) are shown in a cross-sectional view, where $a_1 = a_2 = 1$ mm, $b_1 = b_2 = 0.5$ mm, and $c_2 = 45^\circ \times 0.2$ mm.

Table 2. Production details.*

No.	Type	Diameter (mm)	Tip	Surface	R_a (μm)
1	Steel (c)	1	Conical	P	0.13
2	Steel (c)	2	Conical	P	0.08
3	Nitinol (c)	2	Conical	U	0.09
4	Steel (c)	2	Conical	SB	0.66
5	Steel (c)	2	Conical	EDM	8.21
6	Steel (c)	2	Conical	EDM	41.20
7	Trocar 18G	1.3	Diamond	U	0.39
8	Chiba 22G	0.7	Bevel	U	0.35
	Steel reference (c)	—	—	P	0.10

* All custom-made needles (c) were constructed from stainless steel (Steel), except for needle 3, which was made from superelastic nitinol (Nitinol). The FG_s surface treatment was either polishing (P), sandblasting (SB) or electric discharge machining (EDM). The remaining needles were considered to have an unknown/untreated (U) surface quality.

Table 3. Definition of constants used in the MATLAB video processing functions.

Constant	Value	Unit	Description
$\Delta\theta$	[25,30, ...,180]	°	Evaluated angular range
l_n	45	mm	Evaluated needle length
l_{FGt}	2	mm	FG_t (tip) sample length
l_{FGs}	20	mm	FG_s (shaft) sample length
d_{FG}	See Table 2	mm	FG sample width equal to needle diameter
d_{BG}	2	mm	BG sample width
d_s	2	mm	Distance between FG and BG samples
d_R	100	pixels	Size used in ROI construction
s_{ROI}	d_R, $2d_R$	pixels	Dimensions of ROI: Δx_r, Δy_r
s_{ref}	2, 10	mm	Dimensions of reference specimen: Δx,Δy
i_p	50	—	Array length for a peak search function

BG = background; FG = foreground; ROI = region of interest.

imaged needle. A rotation matrix generated tip position estimates, $\hat{p}$, per image frame, n, according to the equation

$$\hat{p}(n) = \begin{bmatrix} \hat{p}_x(n) \\ \hat{p}_y(n) \end{bmatrix} = \begin{bmatrix} \cos\theta(n) & -\sin\theta(n) \\ \sin\theta(n) & \cos\theta(n) \end{bmatrix} \cdot \begin{bmatrix} \hat{p}_x(0) \\ \hat{p}_y(0) \end{bmatrix} \quad (1)$$

Here, $\begin{bmatrix} \hat{p}_x(0) \\ \hat{p}_y(0) \end{bmatrix}$ was the tip position in one of the manually segmented image frames ($n = 0$), and $\theta(n)$ was the angle between this needle and the desired angle for image frame n.

A rotated region of interest, ROI(n), was defined by $\hat{p}(n)$ and $\theta(n)$, in such a way that the needle was oriented horizontally and that $\hat{p}' = \begin{bmatrix} \hat{p}'_{x'} \\ \hat{p}'_{y'} \end{bmatrix} = \begin{bmatrix} 50 \\ 50 \end{bmatrix}$. The primes indicate the use of the local frame of ROI(n), in which the tip position *estimate* was fixed. Exemplar ROIs are illustrated in Figure 3. From each ROI, FG and BG samples were collected in a series of image processing steps.

Image processing algorithm

A flowchart of sequential processing functions is shown in Figure 4. The outputs were the image samples of the tip, I_{FGt}, shaft, I_{FGs}, tissue, I_{BG} and the observed tip position, $p'(n)$. The algorithm outputs are visualized in Figure 5 for one of the measurements in PVA. Input variables were $\{n, \text{ROI}(n), p'(n-1)\}$. For $n > 1$, the observed position in the last frame acted as an update for the tip position estimate, that is, $\hat{p}'(n) = p'(n-1)$. The main function blocks included filtering, line fitting and intensity analysis steps.

ROI filtering

The black BGs of the measurements in water did not require any image filtering steps. The ROI filtering algorithm was reduced to a single step in which all pixel values that were situated a distance d_s from $\hat{p}_{x'}(n)$ were set to zero. This narrowing of the ROI was used to trim reverberations.

The filtering algorithm was elaborated for the runs in PVA to accommodate robust use in heterogeneous and noisy structures. A filtering mask was created to penalize intensity values away from the needle estimate. This weakened reverberation artifacts and made the approach more conservative. The mask was composed of two parabolic functions that affect the ROI rows and columns, respectively

$$f_{p1}(x', n) = -\left(\frac{x' - (\hat{p}_{x'}(n) - d_s)}{d_s}\right)^2 + 2 \cdot \frac{x' - (\hat{p}_{x'}(n) - d_s)}{d_s}, \quad \text{for } x' \in \mathbb{N} : 1 \le x' \le d_R \quad (2)$$

$$f_{p2}(y') = -\left(\frac{2y'}{d_R}\right)^2 + \frac{4y'}{d_R}, \text{ for } y' \in \mathbb{N} : 1 \le y' \le \frac{d_R}{2} \quad (3)$$

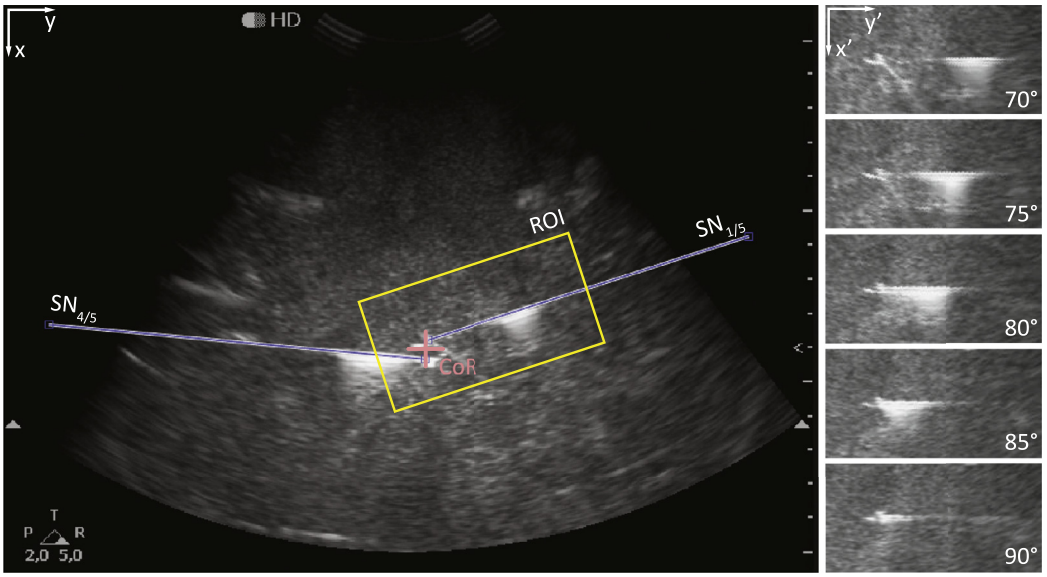

Fig. 3. Left: Overlap of the two US frames used in the manual needle segmentation step. The manual inputs are indicated by the lines $SN_{1/5}$ and $SN_{4/5}$. The average tip position yielded a center of rotation (CoR) in the imaging plane. Local coordinate systems defined the regions of interest (ROI_n). Exemplar ROIs for the angles 70˚, 75˚, . . ., 90˚ are shown on the right. In this range, specular reflections run from the right to the left side in the ROI. This effect is caused by the curved placement of the array elements in the transducer.

The filtering mask is shown in Figure 5b and a processed ROI in Figure 5c. The values for d_s and d_R are specified in Table 3. The peak of f_{p1} has a value of 1 and is located at $\hat{p}_{x'}(n)$. The function roots are a distance $2d_s$ apart. Values of f_{p1} below zero were automatically clipped. The filtered image, ROI_f, was subsequently derived from

$$ROI_f(n) = ROI(n) \cdot f_{p1}(n) \cdot f_{p2} \quad (4)$$

Line fitting

Linear indexing of $ROI_f(n)$ was useful in creating a single data array that resembled a concatenation of needle cross sections. This array was subjected to a peak search function, and the median position of the i_p highest intensity peaks gave a zero polynomial constant, c_0. The resulting needle model is described by the equation

$$f_{needle}(n) = c_0(n) \quad (5)$$

The advantage of this notation is that it allows for a swift code extension to higher polynomial orders, for example, to assess needles that follow a curved trajectory.

Intensity scan

The intensity values along $f_{needle}(n)$ were analyzed to find $p'(n)$; the image samples $I_{FGt}(n)$, $I_{FGs}(n)$ and

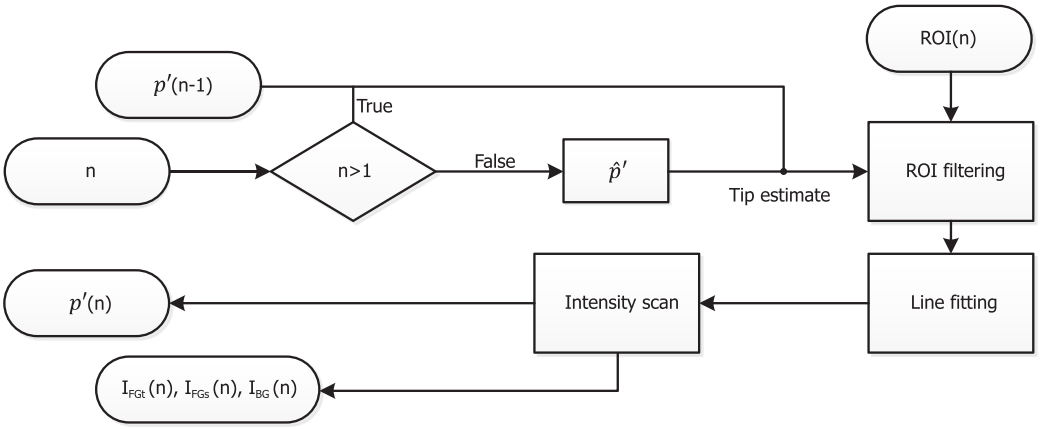

Fig. 4. Image analysis flowchart with frame number n, tip estimate and ROI(n) as inputs. The image intensity samples and an update of the tip position were outputs. The main functions included ROI filtering, line fitting and intensity scan steps. ROI = region of interest.

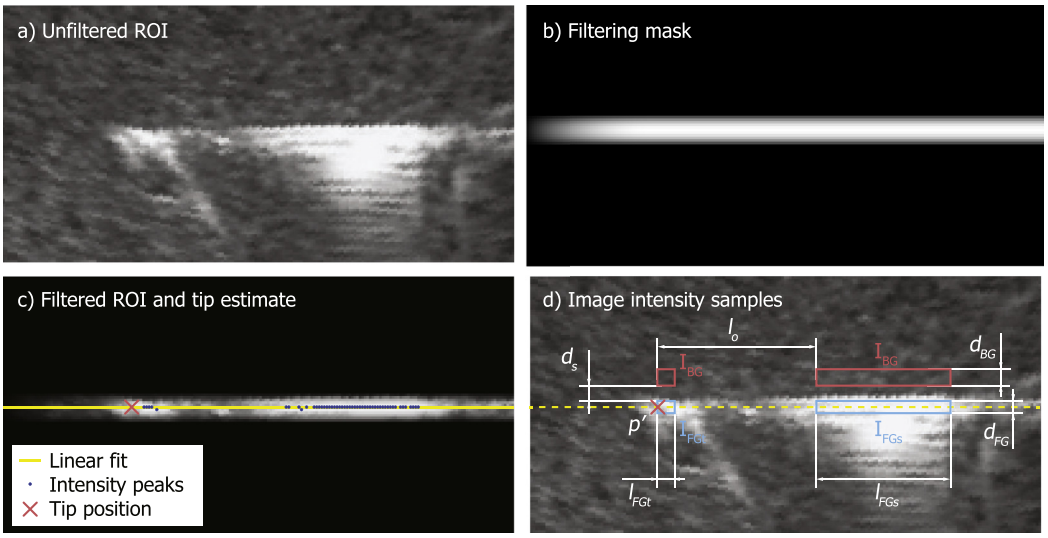

Fig. 5. Image processing steps in PVA, revealing (a) the unfiltered ROI; (b) the filtering mask; (c) the filtered ROI including the line-fitting results based on the i_p peaks and the tip position; and (d) the derived image intensity samples I_{FGt}, I_{FGs} and I_{BG}. The tip position of p' and offset l_0 were derived from intensity scans. ROI = region of interest.

$I_{BG}(n)$; and their mean intensity values $\bar{I}_{FGt}(n)$, $\bar{I}_{FGs}(n)$ and $\bar{I}_{BG}(n)$. A scanning region, ROI_s, was constructed using

$$f_{p3}(y') = \begin{cases} (d_R - y')/d_R & \text{for } y' \in \mathbb{N} : 1 \le y' \le d_R \\ 0 & \text{for } y' \in \mathbb{N} : y' > d_R \end{cases} \quad (6)$$

$$ROI_s(n) = ROI_f(n) \cdot f_{p3} \quad (7)$$

Here, the function f_{p3} decreased linearly from 1 to 0 within the first d_R values. This step enacts an intensity search preference, as we know the tip will be pointing to the left.

To find the tip position, a moving average was computed along $f_{needle}(n)$ in $ROI_s(n)$. A search window (l_{FGt}, d_{FG}) ran in the range $\min\{\hat{p}_{y'}(n-2), \ldots, \hat{p}_{y'}(n)\} + [-2l_{FGt}, 2l_{FGt}]$. The min function made this range conservative in case echogenic tissue structures temporarily obscured the tip. The location, $p_{y'}(n)$, of the highest average intensity, $\bar{I}_{FGt}(n)$, completed $p'(n)$, in accordance with

$$p'(n) = \begin{bmatrix} c_{0(n)} \\ p_{y'(n)} \end{bmatrix} \quad (8)$$

The offset, $l_0(n)$, between the tip and I_{FGs} was found in a second moving average that was computed along $f_{needle}(n)$, this time in $ROI_f(n)$. A search window (l_{FGs}, d_{FG}) ran along the remaining needle length, $[p_{y'}(n) + l_{FGt}, p_{y'}(n) + l_n]$. The location of the highest average intensity, $\bar{I}_{FGs}(n)$, provided $l_0(n)$. All image intensity samples were derived from $p'(n)$ and $l_0(n)$ (see Fig. 5d).

In water, four reference measurements were collected, spread out over the experiment. Static image samples of the reference specimen (size s_{ref}, see Table 3) were registered manually and analyzed for 5 s per video. The average image sample intensity was $\bar{I}_{ref} = 235 \pm 8$ (mean ± standard deviation [SD]).

In PVA, $I_{BG}(n)$ samples were collected above the corresponding FG samples, as in Nakagawa et al. (2015). These samples were composed of a horizontal concatenation of two image portions, collected a distance d_s above $I_{FGt}(n)$ and $I_{FGs}(n)$, respectively.

Echogenicity and visibility metrics

The echogenicity of the tip and shaft was evaluated with a SR, according to

$$SR_t(n) = \frac{\bar{I}_{FGt}(n)}{\bar{I}_{ref}(n)} \quad \text{and} \quad SR_s(n) = \frac{\bar{I}_{FGs}(n)}{\bar{I}_{ref}(n)} \quad (9)$$

and the visibility with a CNR, according to

$$CNR_t(n) = \frac{|\bar{I}_{FGt}(n) - \bar{I}_{BG}(n)|}{\sigma_{BG}(n)} \quad \text{and}$$
$$CNR_s(n) = \frac{|\bar{I}_{FGs}(n) - \bar{I}_{BG}(n)|}{\sigma_{BG}(n)} \quad (10)$$

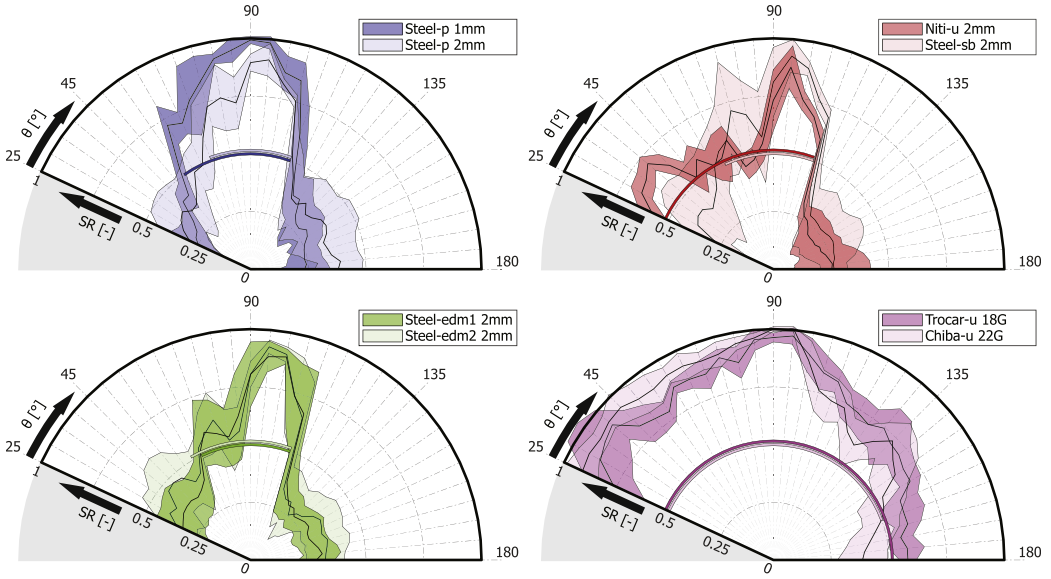

Fig. 6. Polar visualization of needle tip echogenicity, with SR values (radial coordinate) against insertion angles (angular coordinate). The color bands indicate the median ± standard deviation contours. The median range for which SR > 0.5 is represented by arc sections. SR = signal ratio.

Here, σ_{BG} was the SD in the image intensity of sample I_{BG}.

Note that SR = 1 presents the case where the average intensity of the tip or shaft is equal to that of the reference surface.

Methods for data summary and statistical analysis

The comparison of surface treatments consisted of the evaluation of polar data plots, in which the medians ± SD of SR/CNR values were depicted for the $\Delta\theta$ range. A threshold was set at SR = 0.5 or $\tilde{I}_{FG} = 0.5\tilde{I}_{ref}$ to discriminate between a high and a low echogenicity. As a summary value, the high-echoic range was defined by the first and last frames at which the echogenicity was high. These ranges were compared with a Kruskal–Wallis test ($p < 0.05$). Per needle pair, a *post hoc* Mann–Whitney *U*-test was performed.

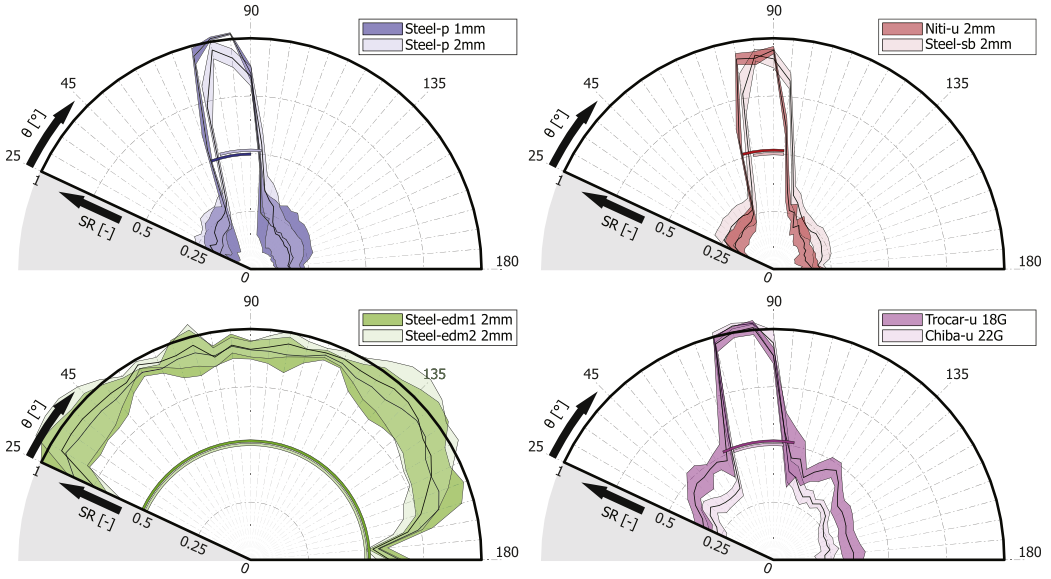

Fig. 7. Polar visualization of needle shaft echogenicity, with SR values (radial coordinate) against insertion angles (angular coordinate). The color bands indicate the median ± standard deviation contours. The median range for which SR > 0.5 is represented by arc sections. SR = signal ratio.

Table 4. Needle tip comparison chart, indicating differences in high-echoic-range median values.

Needle	Range	1	2	3	4	5	6	7	8
1 (Steel-p 1 mm)	55°		*	**	0.16	**	0.38	***	**
2 (Steel-p 2 mm)	43°			*	0.62	0.32	0.76	***	**
3 (Niti-u 2 mm)	85°				*	***	*	***	**
4 (Steel-sb 2 mm)	48°					0.20	0.97	***	*
5 (Steel-edm1 2 mm)	38°						0.18	***	***
6 (Steel-edm2 2 mm)	45°							***	**
7 (Trocar-u 18G)	155°								***
8 (Chiba-u 22G)	133°								

Mann−Whitney *U*-test: *$p < 0.05$, **$p < 0.01$, and ***$p < 0.001$,

RESULTS

The needle tip and shaft echogenicity are visualized in Figures 6 and 7, respectively. Most plots exhibit distinct peaks near the 90° angle, resulting from specular reflections returning to the US transducer.

The data indicate that the beveled (Chiba) and diamond (Trocar) tips of the commercially available needles had a high SR for nearly the full range of angles. In contrast, the high-echoic range of the custom-made conical tips was much smaller. The nitinol tip gave high SR values (≥0.5) for the first half of the angular range. The data and statistical test results are summarized in Table 4.

Low SD values of the needle shaft echogenicity indicate good data reproducibility. The highest return rates of specular reflections (SR peaks) typically occurred near the 80°angle, which can be attributed to the use of a curved-array transducer, together with the fact that I_{FGs} samples were collected somewhat to the right (off-center) in the US image.

The EDM-treated needles had the largest high-echoic range. It equaled the evaluated angular range. The Trocar needle shaft outperformed the Chiba shaft. In turn, the Chiba shaft was better than the other custom-made needles (see Table 5). Also in the low-echoic regions, the SR values of the commercially available needles seemed higher than those of needles 1−4.

No differences were observed between EDM-treated needles ($p = 0.37$). In addition, no differences were found among tested levels in surface roughness (Steel-p 2 mm vs. Steel-sb 2 mm), needle diameter (Steel-p 2 mm vs. Steel-p 1 mm) and material type (Steel-p 2 mm vs. Niti-u 2 mm).

The visibility of the needle tips and shafts in PVA are presented in a similar way, in Figures 8 and 9. The color bands are generally wider, indicating a larger variation (SD) in data values. In agreement with the experiments in water, the Chiba and Trocar needle tips and the EDM-treated shafts resulted in high visibility for the full angular range.

DISCUSSION

In recent years, various needles have been marketed that claim to have echogenic features that locally increase the scattered or specular retroreflection of US waves. However, a methodical approach for the assessment and comparison of these needles has been lacking. Described here is a new and automated method to acquire, analyze and visualize needle echogenicity and visibility in US frames for any pre-selected range and resolution of insertion angles. The initiation and synchronization of the stepper motor and video capturing device required two manual segmentations. The analysis makes use of the unwavering mechanical properties of water and stainless steel (the reflection standard) to

Table 5. Needle shaft comparison chart, indicating differences in high-echoic-range median values.

Needle	Range	1	2	3	4	5	6	7	8
1 (Steel-p 1 mm)	20°		0.96	0.62	0.14	***	***	***	**
2 (Steel-p 2 mm)	20°			0.58	0.08	***	***	***	**
3 (Niti-u 2 mm)	20°				*	***	***	***	**
4 (Steel-sb 2 mm)	15°					***	***	***	**
5 (Steel-edm1 2 mm)	155°						0.37	***	***
6 (Steel-edm2 2 mm)	155°							***	***
7 (Trocar-u 18G)	35°								**
8 (Chiba-u 22G)	25°								

Mann−Whitney *U*-test: *$p < 0.05$, **$p < 0.01$ and ***$p < 0.001$.

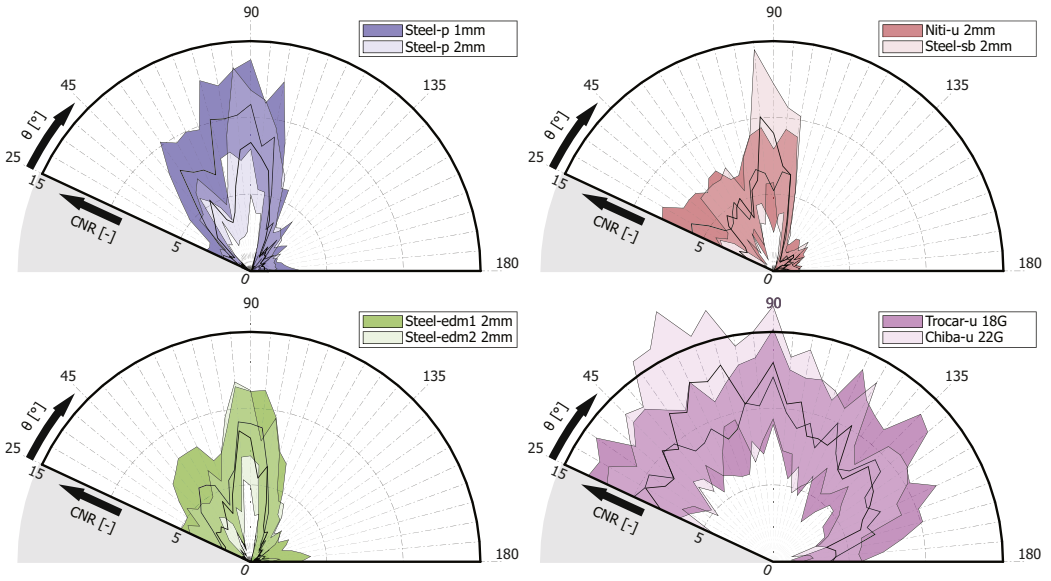

Fig. 8. Polar visualization of needle tip visibility, with CNR values (radial coordinate) against insertion angles (angular coordinate). The color bands indicate the median ± standard deviation contours. CNR = contrast-to-noise ratio.

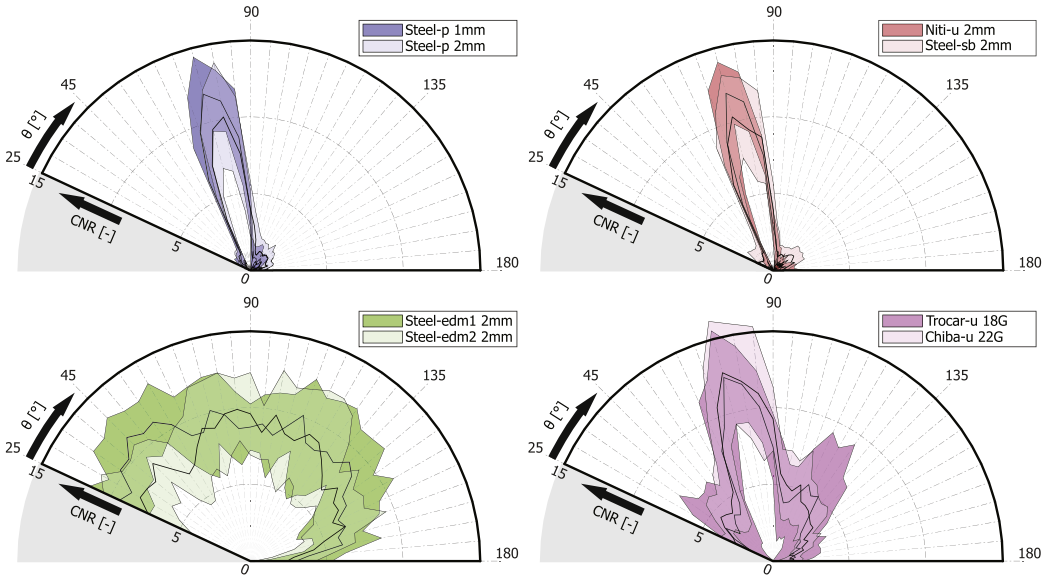

Fig. 9. Polar visualization of needle shaft visibility, with CNR values (radial coordinate) against insertion angles (angular coordinate). The color bands indicate the median ± standard deviation contours.

secure a repeatable process. An in-progress and high-fidelity extension of this work includes *ex vivo* specimens embedded in rotating cylindrical gelatin blocks.

Although the methods described are efficient and new, the results obtained are in line with the literature and expectations. Insertion angle acuteness strongly affected needle visibility (Nichols et al. 2003), and kerfs or grooves increased visibility (Bigeleisen et al. 2016; van de Berg et al. 2018). The conical tips had poor echogenic performance, which may result from a low rate of reflections returning from a convex tip surface.

The relatively good performance of the Chiba and Trocar needle shafts could not be directly attributed to surface roughness, needle diameter or needle material. Other factors that may interact with echogenicity, but

were not studied, include a miniature air gap between the needle stylet and cannula or the presence of any lubrication layers or coatings.

The main limitation of this work is the absence of a clinical criterion for needle visibility. The threshold value SR = 0.5 was used to evenly discriminate high from low reflective signal strengths. This was a mathematically valid, but clinically arbitrary choice. Ideally, threshold values should be established in high-fidelity environments that are also highly reproducible. These conditions are currently unavailable.

Because vision parameters, such as contrast sensitivity, vary between individuals, needle visibility is subject dependent. Furthermore, users can train to look for particular visual cues. For instance, users may estimate the needle position based on tissue motion or distortion. These notions were reflected by numerous user rating-based studies in Table 1. Variations in perception are highly relevant for the clinical task, but they interfere with the study of technical developments. This motivated the focus on measurable differences in the image.

Because of the post-processing nature of this work, it was considered unnecessary to automatically synchronize the operations of the stepper motor and video capturing device. As a result, initial estimates for the search area and insertion angle relied on manual inputs. These estimates may also be obtained by Hough transforms (Okazawa et al. 2006) or optical flow analysis (Bouguet 2000). This may enable real-time needle visibility assessments, which can be of use in 3-D US slice detection or in uncertainty-based motion planning for steerable needles (Alterovitz et al. 2008).

CONCLUSIONS

This article describes systematic methods to acquire, analyze and display the visibility and echogenicity of needles in US images for a full range of insertion angles. The approach was based on a contrast-to-noise ratio and a SR, respectively. An evaluation study was included to compare the effects of various needle surface treatments. The data are presented by contour plots that intuitively discriminate between needles with a wide or a narrow high-echoic range. The best performance was attributed to the Trocar and Chiba needle tips and to the EDM-treated shafts. These shafts simulated flexure joint structures, which can be found in steerable needles.

Acknowledgments—This work was supported by the ZonMW program Innovative Medical Devices Initiative (IMDI) Life Sciences and Health (No.104003015).

SUPPLEMENTARY DATA

Supplementary data related to this article can be found at doi:10.1016/j.ultrasmedbio.2018.10.004.

REFERENCES

Abbal B, Choquet O, Gourari A, Bouic N, Massone A, Biboulet P, Bringuier S, Capdevila X. Enhanced visual acuity with echogenic needles in ultrasound-guided axillary brachial plexus block: A randomized, comparative, observer-blinded study. Minerva Anestesiol 2015;81:369–378.

Adebar TK, Fletcher AE, Okamura AM. 3-D ultrasound-guided robotic needle steering in biological tissue. IEEE Trans Biomed Eng 2014;61:2899–2910.

Alterovitz R, Branicky M, Goldberg K. Motion planning under uncertainty for image-guided medical needle steering. Int J Robot Res 2008;27:1361–1374.

Arif M, Moelker A, van Walsum T. Needle tip visibility in 3D ultrasound images. Cardiovasc Interv Radiol 2018;41:145–152.

Baker JA, Soo MS, Mengoni P. Sonographically guided percutaneous interventions of the breast using a steerable ultrasound beam. Am J Roentgenol 1999;172:157–159.

Bergin D, Pappas JN, Hwang JJ, Sheafor DH, Paulson EK. Echogenic polymer coating: Does it improve needle visualization in sonographically guided biopsy?. Am J Roentgenol 2002;178:1188–1190.

Bigeleisen PE, Hess A, Zhu R, Krediet A. Modeling, production, and testing of an echogenic needle for ultrasoundguided nerve blocks. J Ultrasound Med 2016;35:1319–1323.

Bouguet J. Pyramidal implementation of the Lucas−Kanade feature tracker. OpenCV document, Intel, Microprocessor Research Labs; 2000.

Cabreros SS, Jimenez NM, Greer JD, Adebar TK, Okamura AM. Remote electromagnetic vibration of steerable needles for imaging in power doppler ultrasound. IEEE Int Conf Robot Autom 2015;2015:2244–2249.

Chapman GA, Johnson D, Bodenham AR. Visualisation of needle position using ultrasonography. Anaesthesia 2006;61:148–158.

Charboneau JW, Reading CC, Welch TJ. CT and sonographically guided needle-biopsy—Current techniques and new innovations. Am J Roentgenol 1990;154:1–10.

Cohnen M, Saleh A, Luthen R, Bode J, Modder U. Improvement of sonographic needle visibility in cirrhotic livers during transjugular intrahepatic portosystemic stent-shunt procedures with use of real-time compound imaging. J Vasc Interv Radiol 2003;14:103–106.

Culp WC, McCowan TC, Goertzen TC, Habbe TG, Hummel MM, LeVeen RF, Anderson JC. Relative ultrasonographic echogenicity of standard, dimpled, and polymeric-coated needles. J Vasc Interv Radiol 2000;11:351–358.

de Jong TL, Pluymen LH, van Gerwen DJ, Kleinrensink GJ, Dankelman J, van den Dobbelsteen JJ. PVA matches human liver in needle−tissue interaction. J Mech Behav Biomed Mater 2017;69:223–228.

de Jong TL, van de Berg NJ, Tas L, Moelker A, Dankelman J, van den Dobbelsteen JJ. Needle placement errors: Do we need steerable needles in interventional radiology? Med Devices Evidence Res 2018;11:259–265.

de Korte CL, Weijers G, Vriezema DM, Keereweer AR, Thijssen JM, Hansen HHG. Quantitative analysis of coated needles for ultrasound guided intervention. Proc IEEE Int Ultrason Symp 2012;1571–1574.

Edgcombe H, Hocking G. Sonographic identification of needle tip by specialists and novices a blinded comparison of 5 regional block needles in fresh human cadavers. Reg Anesth Pain Med 2010;35:207–211.

Fuzier R, Casalprim J, Bataille B, Harper I, Magues JP. The echogenicity of nerve blockade needles. Anaesthesia 2015;70:462–466.

Gofeld M, Krashin DL, Ahn S. Needle echogenicity in ultrasound-guided lumbar spine injections: A cadaveric study. Pain Physician 2013;16:E725–E730.

Gottlieb RH, Robinette WB, Rubens DJ, Hartley DF, Fultz PJ, Violante MR. Coating agent permits improved visualization of biopsy needles during sonography. Am J Roentgenol 1998;171:1301–1302.

Guo S, Schwab A, McLeod G, Corner G, Cochran S, Eisma R, Soames R. Echogenic regional anaesthesia needles: A comparison study in thiel cadavers. Ultrasound Med Biol 2012;38:702–707.

Harmat A, Rohling RN, Salcudean SE. Needle tip localization using stylet vibration. Ultrasound Med Biol 2006;32:1339–1348.

Hebard S, Hocking G, Murray K. Two-dimensional mapping to assess direction and magnitude of needle tip error in ultrasound-guided regional anaesthesia. Anaesth Intensive Care 2011;39:1076–1081.

Henken KR, Seevinck PR, Dankelman J, van den Dobbelsteen JJ. Manually controlled steerable needle for MRI-guided percutaneous interventions. Med Biol Eng Comput 2017;55:235–244.

Kilicaslan A, Topal A, Tavlan A, Erol A, Otelcioglu S. Differences in tip visibility and nerve block parameters between two echogenic needles during a simulation study with inexperienced anesthesia trainees. J Anesth 2014;28:460–462.

Klein SM, Fronheiser MP, Reach J, Nielsen KC, Smith SW. Piezoelectric vibrating needle and catheter for enhancing ultrasound-guided peripheral nerve blocks. Anesth Analg 2007;105:1858–1860.

Künzli BM, Abitabile P, Maurer CA. Radiofrequency ablation of liver tumors: Actual limitations and potential solutions in the future. World J Hepatol 2011;3:8–14.

Maecken T, Zenz M, Grau T. Ultrasound characteristics of needles for regional anesthesia. Reg Anesth Pain Med 2007;32:440–447.

Mariano ER, Yun RDH, Kim TE, Carvalho B. Application of echogenic technology for catheters used in ultrasound-guided continuous peripheral nerve blocks. J Ultrasound Med 2014;33:905–911.

Mesurolle B, Bining HJS, El Khoury M, Barhdadi A, Kao E. Contribution of tissue harmonic imaging and frequency compound imaging in interventional breast sonography. J Ultrasound Med 2006;25:845–855.

Miura M, Takeyama K, Suzuki T. Visibility of ultrasound-guided echogenic needle and its potential in clinical delivery of regional anesthesia. Tokai J Exp Clin Med 2014;39:80–86.

Munirama S, Joy J, Columb M, Habershaw R, Eisma R, Corner G, Cochran S, McLeod G. A randomised, single-blind technical study comparing the ultrasonic visibility of smooth-surfaced and textured needles in a soft embalmed cadaver model. Anaesthesia 2015;70:537–542.

Nakagawa K, Kamiya T, Arakawa K, Akiyama S, Sakai K. Objective and subjective comparison of the visibility of three echogenic needles and a nonechogenic needle on older ultrasound devices. Acta Anaesthesiol Taiwan 2015;53:1–6.

Nichols K, Wright LB, Spencer T, Culp WC. Changes in ultrasonographic echogenicity and visibility of needles with changes in angles of insonation. J Vasc Interv Radiol 2003;14:1553–1557.

Okazawa SH, Ebrahimi R, Chuang J, Rohling RN, Salcudean SE. Methods for segmenting curved needles in ultrasound images. Med Image Anal 2006;10:330–342.

Reading CC, Charboneau JW, Felmlee JP, James EM. US-guided percutaneous biopsy—Use of a screw biopsy stylet to aid needle detection. Radiology 1987;163:280–281.

Schafhalter-Zoppoth I, McCulloch CE, Gray AT. Ultrasound visibility of needles used for regional nerve block: An in vitro study. Reg Anesth Pain Med 2004;29:480–488.

Surry KJM, Austin HJB, Fenster A, Peters TM. Poly(vinyl alcohol) cryogel phantoms for use in ultrasound and MR imaging. Phys Med Biol 2004;49:5529–5546.

Sviggum HP, Ahn K, Dilger JA, Smith HM. Needle echogenicity in sonographically guided regional anesthesia blinded comparison of 4 enhanced needles and validation of visual criteria for evaluation. J Ultrasound Med 2013;32:143–148.

Uppal V, Sondekoppam RV, Ganapathy S. Effect of beam steering on the visibility of echogenic and non-echogenic needles: a laboratory study. Can J Anaesth 2014;61:909–915.

van de Berg NJ, Dankelman J, van den Dobbelsteen JJ. Endpoint accuracy in manual control of a steerable needle. J Vasc Interv Radiol 2017;28:276–283.

van de Berg NJ, Sánchez-Margallo JA, Langø T, van den Dobbelsteen JJ. Compliant joint echogenicity in ultrasound images: towards highly visible steerable needles. In: Proc SPIE 10576, Medical Imaging 2018: Image-Guided Procedures, Robotic Interventions, and Modeling, 105760X. doi: 10.1117/12.2293501.

Wiesmann T, Borntrager A, Zoremba M, Neff M, Wulf H, Steinfeldt T. Compound imaging technology and echogenic needle design effects on needle visibility and tissue imaging. Reg Anesth Pain Med 2013;38:452–455.